Ocean Engineering 341 (2025) 122659

Contents lists available at ScienceDirect

Ocean Engineering

journal homepage: www.elsevier.com/locate/oceaneng

Research paper

An approach to estimate vertical center of gravity, draught and RAO from ship motions based on prolate spheroidal wave functions and time-series filtering

Malwin Wermbter *, Robinson Perić, Johanna Serr, Moustafa Abdel-Maksoud

Institute for Fluid Dynamics and Ship Theory, Hamburg University of Technology, Am Schwarzenberg-Campus 4, Hamburg, 21073, Hamburg, Germany

ARTICLE INFO

Keywords:
Center-of-gravity estimation
Draught estimation
Response amplitude operator
Time series filtering
Prolate spheroidal wave functions
Ship motion measurements

ABSTRACT

The motion behavior of a ship is significantly influenced by its draught and the position of the vertical center of gravity (VCG). Accurate estimation of these two parameters enables determination of the response amplitude operator (RAO). This study presents a method to estimate draught, VCG, RAO and wave spectral parameters based on prolate spheroidal wave functions and time-series filtering. The method requires only measured motion data and predefined RAOs as input. Validation is performed by comparing the estimated parameters with known reference values from numerical simulations and model tests. A main contribution is the automated identification of time windows with high estimation accuracy. For numerical and model test cases, RAO, VCG and draught showed deviations of approximately 15 %. The accuracy of the applied RAO database and non-linearities are the main source of uncertainty. Estimations required a few hours of measurements in full-scale. Application to full-scale measurements provides predictions with comparable accuracy to which obtained numerically, indicating that real-time onboard application is possible.

1. Introduction

Knowledge of the ship mass distribution is highly important to determine the motion behavior of ships in service. Two key parameters governing this behavior are the vertical center of gravity (VCG) and the ship's draught (D), which is related to the ship's mass. Both parameters vary during ship operation, but are required to carry out online estimates of the ship's response amplitude operators (RAOs) with high accuracy. The RAO is denoted with $\hat{Y}$ in this work and relates the complex motion amplitude $\hat{r}$ to the complex wave excitation $\hat{\zeta}$ with the ratio $\hat{Y} = \hat{r}/\hat{\zeta}$ at a given frequency ω, encounter angle μ and degree of freedom (DOF). Especially for ships with varying loading conditions, the RAO changes significantly for each voyage. The RAO is required for applications such as sea state estimations with ship-as-a-wave-buoy methods (or wave-buoy analogy, WBA), digital twins for risk mitigation (e.g. parametric roll, container losses) as well as algorithms for route optimization.

This work focuses on determining VCG, draught and RAO from ship motion time series. Existing approaches can be categorized into data-driven models, RAO-tuning techniques, and physics-based identification methods.

Data-driven methods can estimate sea state parameters without requiring exact knowledge of the VCG and draught, as long as the database contains training data representing the current state. These methods typically determine the wave integral parameters such as significant wave height H_s, peak period T_p and encounter angle μ. Mak and Düz (2019) compared multiple convolutional neural networks (CNNs) and predicted the wave encounter angle with mean deviations below 1° and 95 % confidence intervals around 30°. They state that a broad and representative data base is required, which limits the methods applicability to multiple ships. Mittendorf et al. (2022) compared multiple machine learning architectures and determined the wave integral parameters with lowest root mean square errors for the encounter angles of 10°, but concluded that a hybrid-approach of a physics-based and a data-driven method may be superior due to the reduced amount of required training data. Since data-driven methods depend on the quality and quantity of training data, their application to onboard estimation on ships with varying loading conditions is challenging, especially due to the fact that storms and critical ship motions are rare.

RAO-Tuning methods require a weather report and an initial RAO to minimize the difference between the measured and estimated response spectrum of the ship motion. Nielsen et al. (2021) optimizes a

* Corresponding author.
E-mail addresses: malwin.wermbter@tuhh.de (M. Wermbter), robinson.peric@tuhh.de (R. Perić), johanna.serr@tuhh.de (J. Serr), m.abdel-maksoud@tuhh.de (M. Abdel-Maksoud).

https://doi.org/10.1016/j.oceaneng.2025.122659
Received 17 June 2025; Received in revised form 19 August 2025; Accepted 29 August 2025
Available online 15 September 2025

frequency and encounter angle dependent factor in order to minimize the difference between the response spectra. The response spectra difference with the tuned RAO is smaller than using a normal RAO. Mounet et al. (2024) employed evolutionary algorithms to derive optimal RAOs from parametrized RAOs (pRAOs). The derived pRAOs were valid for all encounter angles. The application to full-scale data with weighting of specific data segments resulted in up to 50 % deviating response spectra areas, showing highest uncertainty for the non-linear roll motion. Han et al. (2021) implemented Bayesian updating of the RAO, which requires a RAO database. Takami et al. (2024b, 2025) recently published a method based on prolate spheroidal wave functions (PSWF) to derive the amplitude and phase of the RAO with negligible difference from synthetic data without requiring weather data . However, these methods still rely on existing data and may struggle with generalization, particularly for accuracy in under-represented sea states or when non-linear effects dominate the response which are not covered by RAOs.

Physic-based methods aim to estimate the parameters defining the RAOs, in this case the VCG and draught. These are typically identified by minimizing the error between measured motions and theoretical motion models. Deriving parameters influencing the RAOs is advantageous, since it allows to determine a RAO from a database. While such methods are well established in the automotive and aerospace sector (Al-Rawashdeh et al., 2014, 2023; Fathy et al., 2008; Wittmer et al., 2023; Stanley and Goodall, 2009). the applied methods require additional measurements not available for ships, for example force measurements on the hull surface.

Some physics-based approaches use only motion measurements, but make use of strong simplifications. Chhoeung and Hahn (2019) proposed the application of design formulae to estimate the VCG from the measured roll period from heeling tests, but these formulae assume static conditions, which are not valid in open seas as well as non-conventional hull forms. One common assumption is that the VCG coincides with the vertical center of rotation (VCR). Javanmardi (2024) applied relative kinematics to determine the VCR from multiple motion measurements with numerical and full-scale measurements. Correlations of 0.9 and greater between measured and predicted heave motions are reported, but differences in VCR position of up to 15 % were observed with measurement data. Abankwa et al. (2018) presented a similar approach to determine the longitudinal center of rotation (LCR) showing uncertainty up to 20 %. However, it is known that the LCR varies from the LCG (de Oliveira et al., 2018) and the VCR varies from the VCG (Fernandes et al., 2016). The VCR for ships in waves varies with time and sea state for some time instants up to 50 % (Johnsen and Krüger, 2021; Zhang, 2022). Therefore, the methods assuming that VCR is equal to VCG seem not to be suitable for accurate VCG estimation.

This study proposes a novel physics-based approach for VCG, draught and RAO estimation that relies solely only motion measurements building upon the method using PSWF from Takami et al. (2022). Unlike data-driven and RAO-tuning methods, this approach requires significantly smaller data sets. Using only motion measurements is beneficial for application onboard of ships and using PSWF avoids the need of calibration data sets. There is no need to assume that the VCR corresponds to the VCG. The PSWF method is able to reconstruct ship motions and wave profiles in time domain. Takami et al. (2023, 2024a) have shown that the method is reliable in determining wave spectral parameters, wave profiles and roll damping parameters with synthetic data. The contribution of this study is the extension of the PSWF method to estimate the VCG and draught. It is achieved by using the formulae for wave encounter angle estimation in a similar form for the VCG and draught estimation. Special emphasis is placed on real-world applicability, with a focus on achieving accurate results from noisy measurements across varying sea states. Therefore, a methodology is developed which automatically identifies time windows delivering highly accurate estimates without additional input. The approach is validated with numerical, model test data from a barge, whose full-scale measurements are used to apply the method and showcase the practicability.

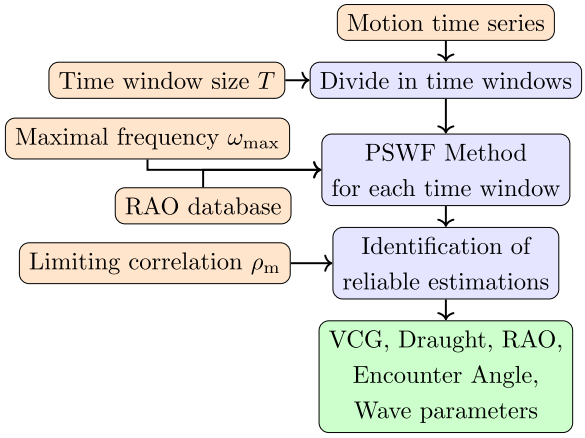

Fig. 1. Schematic VCG and draught estimation procedure with inputs in orange, calculations in blue and results in green.

This article is organized as follows. Section 2 contains the PSWF method and the procedure to obtain estimates from measurement data is explained. Section 3 describes the measurement data which is used in Section 4 for validation and application. Section 5 outlines key findings and discusses limitations. Section 6 summarizes the study and future work.

2. Methods

The section is structured into three subsections to estimate VCG and draught based on the PSWF method.

The workflow is shown in Fig. 1. Section 2.1 introduces the required transformations for converting the data obtained by inertial measurement unit (IMU) for accelerations and angular velocities into rigid-body motion time series. Section 2.2 sets up the PSWF method which is executed for each time window to gain an estimate for VCG, draught, RAO and wave spectral parameters each. Section 2.3 uses these estimates to identify reliable estimations with high accuracy. Inputs to the methodology are three user-selected scalars: the time window size T, a maximal frequency $\omega_{\max}$ and a limiting correlation ρ_{m}. The input motions data sets are measured or numerically calculated and the RAO database is obtained using a frequency domain method.

2.1. Calculation of rigid body motions using inertial measurement unit data

Reconstruction of motions with PSWF requires signals of multiple DOF. An inertial measurement unit (IMU) provides a low-cost solution to measure accelerations and angular velocities. To apply the PSWF method, these measurements have to be integrated in time and transformed to the center of gravity (CG), where the RAOs are defined. The measurements are given in a ship-fixed coordinate system, while ship motions are described in the hydrodynamic coordinate system (Perez, 2006). The hydrodynamic coordinate system moves with the ship's average forward speed along the water surface. Its x-axis points forward, y-axis to starboard and z-axis downward. The ship-fixed coordinate system is attached to the CG and performs all translations and rotations. The x-axis points forward to the bow, the y-axis to starboard and z-axis downward.

The measured angular velocities by the IMU $\vec{\omega}$ are transformed to hydrodynamic angular velocities $\dot{\vec{\theta}}$ using the relation (Mounet et al., 2024)

$$\dot{\vec{\theta}} = \boldsymbol{T}_{\theta}(\vec{\theta})(\vec{\omega} - \vec{b}_{\theta} - \vec{n}_{\theta}). \tag{1}$$

The measurements are subtracted with sensor bias $\vec{b}_{\theta}$ and white noise $\vec{n}$. The transformation matrix $\boldsymbol{T}_{\theta}$ depends on the current rotation angle

vector $\vec{\theta}$ (Perez, 2006). This equation forms an initial value problem that is integrated using a fourth-order Runge-Kutta scheme.

Accelerations are transformed from the IMU's position (denoted by b) to the CG (denoted by g) using the relative position vector $\vec{x}_{bg} = \vec{x}_g - \vec{x}_b$ and the angular velocities

$$\vec{a}_g = \vec{a}_b + \dot{\vec{\omega}} \times \vec{x}_{bg} + \vec{\omega} \times \vec{\omega} \times (\vec{x}_{bg}). \tag{2}$$

The transformation to the hydrodynamic coordinate system is performed as follows

$$\ddot{\vec{r}} = \boldsymbol{T}(\vec{\theta})(\vec{a}_g - \vec{b}_a - \vec{n}_a) - \vec{g}, \tag{3}$$

where $\boldsymbol{T}(\vec{\theta})$ is the coordinate transformation matrix (Perez, 2006). The acceleration bias $\vec{b}_a$ and noise $\vec{n}_a$ are subtracted. The gravitational acceleration vector $\vec{g}$ is subtracted after the coordinate transformation. The velocities and positions result from numerical integration of the measurement equation.

To reduce signal noise and computational effort, IMU data are downsampled from 40 Hz to 10 Hz. The measurements are then subtracted from noise and bias using a fourth-order low- and high-pass Butterworth filter with cut-off frequencies set to 1 Hz and 0.14 Hz respectively. High-pass filtering is applied before each integration step to prevent drift in the resulting velocities, positions or rotation angles.

This work yields reliable motions for DOFs with restoring forces (i.e. heave, roll, pitch), because these motions oscillate about a known equilibrium position. The accuracy of the motions predicted for surge, sway and yaw is limited, because they are lower frequent and contain drifts, where the applied filters would be to restrictive. Advanced filtering techniques like Kalman filters would be required to calculate motions of these DOF with high accuracy. However, such techniques are not necessary in this study, as the analysis of the heave, roll and pitch data provides sufficient information to estimate VCG and draught.

2.2. Prolate spheroidal wave functions for ship motion reconstruction

This section contains the methodology to obtain estimates for VCG, draught, RAO and the wave parameters with PSWF. Fig. 2 shows the procedure starting with the ship motions, the Froude number Fn and the RAO database as input. Following, the motions are split into time windows. In these windows, the motions are reconstructed and the angle, VCG and draught are estimated afterwards. Based on the obtained wave spectral parameters, the encounter angle is iterated. The procedure results in estimates for each time window of length $2T$. Time windows overlap by 20 % to increase accuracy of wave profile estimation at the boundaries, resulting in a step size of $1.6T$. The procedure is repeated until the full motion signal of length T_m has been processed. Section numbers next to the arrows indicate the sections containing the detailed description of the individual estimation steps.

2.2.1. Reconstruction of ship motion

PSWF are used to reconstruct a signal in the time window $[-T, T]$. In this study, PSWF are used to reconstruct ship motion measurements of an arbitrary degree of freedom k. The main advantage of PSWF in comparison to a Fast Fourier Transform (FFT) is that it is able to reconstruct the motion in short time frames with high accuracy, since the frequency discretisation depends on the selected maximal frequency ω_{max} and not on the time window size (Takami et al., 2022).

Fig. 3 summarises the reconstruction graphically. The time window size T and the upper frequency limit ω_{max} are input parameters. Both parameters are required to calculate the PSWF. As suggested by Boyd (2005), the number of PSWF should be $2N + 30$ to avoid unstable PSWF, where N is the number of Legendre polynomials used to generate a single PSWF. The number of frequencies n used for motion reconstruction is equal to the number of PSWF and is calculated as

$$n = 2 \cdot \underbrace{\left(\frac{2T\omega_{max}}{\pi} - 1 \right)}_{N} + 30. \tag{4}$$

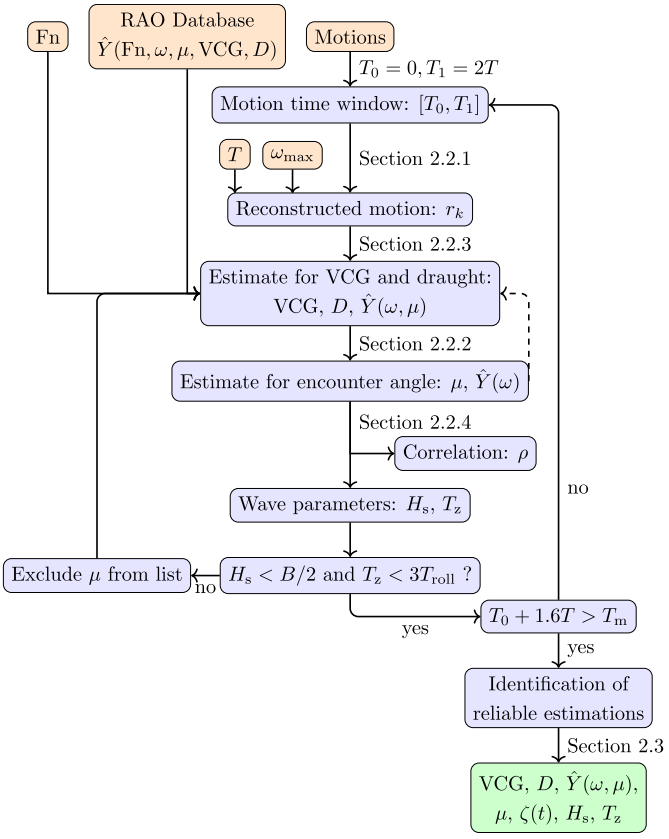

Fig. 2. Detailed VCG and draught estimation procedure with the PSWF method. Input data are orange, calculations are blue and results are green.

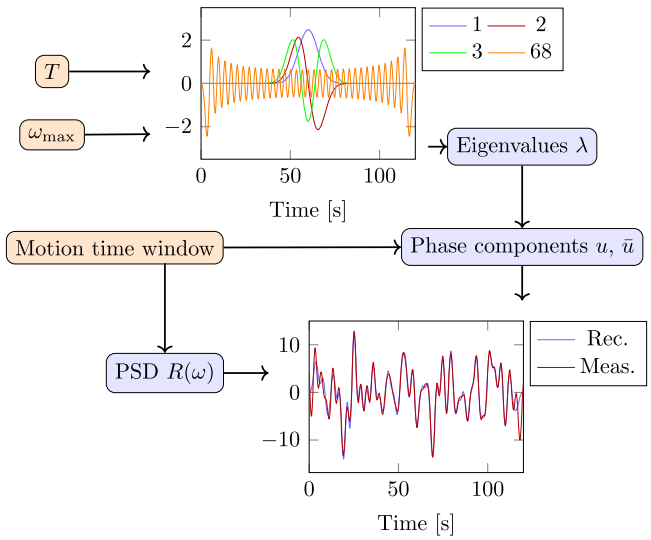

Fig. 3. Reconstruction of motions with PSWF.

The resulting PSWF are shown for order 1 to 3 and exemplarily for order 68, which marks the upper limit with $T = 30$ s and $\omega_{max} = 1\,\mathrm{rad\,s^{-1}}$. The eigenvalues λ of the PSWF and the phase components u and $\bar{u}$ for each frequency up to ω_{max} are calculated as described in Takami et al. (2022). Frequencies above ω_{max} are not accurately reconstructed with PSWF and therefore omitted. Selection of the ω_{max} should therefore be done according to the expected motion frequencies. The reconstruction of a signal with n harmonic functions and a phase shift ε is transformed

as follows

$$r_{\mathrm{k}}(t) \approx \sum_{i=1}^{n} \sqrt{2R_{\mathrm{k}}(\omega_i)\,\Delta\omega}\cos(\omega_{\mathrm{i}} t - \varepsilon_{\mathrm{i,k}}), \tag{5}$$

$$\approx \sum_{i=1}^{n} \sqrt{R_{\mathrm{k}}(\omega_i)\,\Delta\omega}\left(u_{\mathrm{i,k}}\cos(\omega_{\mathrm{i}} t) - \bar{u}_{\mathrm{i,k}}\sin(\omega_{\mathrm{i}} t)\right). \tag{6}$$

The motion response spectrum $R_{\mathrm{k}}(\omega) = 2/\pi \int_0^{2T} \mathrm{ACF}(\tau)\cos(\omega\tau)\,\mathrm{d}\tau$ is computed from the signal's autocorrelation function (ACF) (Kitagawa, 2010). The usage of autocorrelation is beneficial for the short time windows in contrast to the FFT, since windowing effects would influence the results. The frequencies are linearly distributed between a small value, e.g. $1e^{-3}$ and $\omega_{\max}$, with step size $\Delta\omega$. The formulae are applicable to various types of signals. In this study, they are applied to ship translations, rotations and moments around the ship center of gravity.

2.2.2. Estimation of wave encounter angle

The identified phase components by the PSWF method are used to estimate the wave encounter angle. The encounter angle μ is defined such that 0° corresponds to waves coming from stern, 90° from starboard and 180° from bow. Takami et al. (2022) introduced the assumption that a motion may be reconstructed from any other DOF by applying the phase difference of their RAOs $\hat{Y}$. The RAO phase φ is given by

$$\varphi_{\mathrm{i,k}}(\mu) = \arctan\frac{\mathrm{Im}(\hat{Y}(\omega_{\mathrm{i}},\mu))}{\mathrm{Re}(\hat{Y}(\omega_{\mathrm{i}},\mu))}. \tag{7}$$

Inserting the phase difference of DOF k and l into Eq. (6) and taking the sum of all non-identical DOFs yields

$$r_{\mathrm{k}}^{\mu}(t) = \sum_{i=1}^{n}\sum_{\substack{l=1\\ l\neq k}}^{m} \sqrt{R_{\mathrm{k}}(\omega_i)\,\Delta\omega}\left(u_{\mathrm{i},l}\cos(\omega_i t - \varphi_{\mathrm{i,l}}(\mu) + \varphi_{\mathrm{i,k}}(\mu))\right.$$
$$\left. - \bar{u}_{\mathrm{i},l}\sin(\omega_i t - \varphi_{\mathrm{i,l}}(\mu) + \varphi_{\mathrm{i,k}}(\mu))\right). \tag{8}$$

Summing up the resulting signals for all DOFs provides the reconstructed signal r^{μ} for each angle. The correlation ρ^{μ} between the measured and reconstructed signal is calculated with the covariance cov and standard deviation σ

$$\rho^{\mu} = \sum_{k=1}^{m} \frac{\mathrm{cov}(r_{\mathrm{k}}^{\mu}, r_{\mathrm{k}})}{\sigma(r_{\mathrm{k}}^{\mu})\cdot\sigma(r_{\mathrm{k}})}. \tag{9}$$

Correlation values range from −1 indicating an anti-proportional signal and 1 indicating perfect correlation and therefore the same signal. 0 indicates no relationship between the signals. The encounter angle with the highest correlation was sometimes misidentified between starboard and portside. To avoid this ambiguity, the encounter angles are classified into segments of three consecutive encounter angles

$$\bar{\rho}_j = \sum_{i=j-1}^{j+1} \rho^{\mu_{\mathrm{i}}}. \tag{10}$$

The estimated angle μ_{e} was chosen from the center of the segment with the highest total correlation

$$j^* = \underset{j=2,\ldots,n_{\mu}-1}{\arg\max}\left(\bar{\rho}_j\right), \tag{11}$$

$$\mu = \mu_{j^*}. \tag{12}$$

As seen in Fig. 2, based on the wave spectral parameters some angles leading to unfeasible wave heights and zero-upcrossing periods are excluded until plausible wave spectral parameters are calculated.

2.2.3. Estimation of VCG, draught

The estimation of VCG and draught D follows a similar correlation-based approach used for encounter angle estimation. However, unlike the encounter angle selection based on segments in Eq. (10), the optimal combination is selected from all VCG and D correlations $\rho^{\mathrm{VCG},D}$. Eq. (8) is reused by substituting the encounter angle μ with VCG, D. The number of RAOs corresponds to the number of VCGs n_{VCG} multiplied with the number of draughts n_{D}. The optimal quantities are determined by

$$j^* = \underset{j=1,\ldots,n_{\mathrm{VCG}}\cdot n_{\mathrm{D}}}{\arg\max}\left(\rho^{\mathrm{VCG_j},D_{\mathrm{j}}}\right), \tag{13}$$

$$\mathrm{VCG} = \mathrm{VCG}_{j^*}, \quad D = D_{j^*}. \tag{14}$$

Estimation of VCG and draught is performed prior to the estimation of the encounter angle, as shown in Fig. 2. Since the estimation of these parameters requires a value of μ to select the corresponding RAO, the procedure initializes the encounter angle with 90° for the first time window. For all subsequent windows, the previously estimated encounter angle is used.

2.2.4. Estimation of wave profile and spectral parameters

The wave spectrum S_ζ is calculated as established by Takami et al. (2023). For simplicity, the notation of the complex RAOs is shortened to $\hat{Y}_k(\omega_{\mathrm{i}}, \mu_{\mathrm{e}}, \mathrm{VCG}_{\mathrm{e}}, D_{\mathrm{e}}) = \hat{Y}_{\mathrm{i,k}}$ and the same logic is applied to the phase shift of the RAOs

$$S_\zeta(\omega_{\mathrm{i}}) = \frac{\pi}{2T\Delta\omega^2}\left(\frac{\sum_{k=1}^{m}\frac{\sqrt{R_{\mathrm{k}}(\omega_{\mathrm{i}})\Delta\omega}|\hat{Y}_{\mathrm{i,k}}|}{|\hat{Y}_{\mathrm{max,k}}|^2}\left(u_{\mathrm{i,k}}\cos\varphi_{\mathrm{i,k}} + \bar{u}_{\mathrm{i,k}}\sin\varphi_{\mathrm{i,k}}\right)}{\sum_{k=1}^{m}\left(\frac{|\hat{Y}_{\mathrm{i,k}}|}{|\hat{Y}_{\mathrm{max,k}}|}\right)^2}\right)^2$$
$$+ \frac{\pi}{2T\Delta\omega^2}\left(\frac{\sum_{k=1}^{m}\frac{\sqrt{R_{\mathrm{k}}(\omega_{\mathrm{i}})\Delta\omega}|\hat{Y}_{\mathrm{i,k}}|}{|\hat{Y}_{\mathrm{max,k}}|^2}\left(\bar{u}_{\mathrm{i,k}}\cos\varphi_{\mathrm{i,k}} - u_{\mathrm{i,k}}\sin\varphi_{\mathrm{i,k}}\right)}{\sum_{k=1}^{m}\left(\frac{|\hat{Y}_{\mathrm{i,k}}|}{|\hat{Y}_{\mathrm{max,k}}|}\right)^2}\right)^2. \tag{15}$$

To avoid numerical instability due to division by small or zero RAO amplitudes, this formulation is normalized using the maximal amplitude $|\hat{Y}_{\mathrm{max,k}}|$. According to Takami et al. (2022), only frequencies satisfying the condition $\alpha = \frac{|\hat{Y}_{\mathrm{i,k}}|}{|\hat{Y}_{\mathrm{max,k}}|} > 0.1$ are included. The estimation of the time domain wave profile is possible with the PSWF method, but not required for VCG and draught estimation.

From the wave spectrum, the significant wave height H_{s} and zero-upcrossing period T_{z} are computed using standard spectral relations (Journée and Massie, 2001)

$$H_{\mathrm{s}} = 4\sqrt{\int S_\zeta(\omega)\mathrm{d}\omega}, \tag{16}$$

$$T_{\mathrm{z}} = 2\pi\sqrt{\frac{\int S_\zeta(\omega)\mathrm{d}\omega}{\int \omega^2 S_\zeta(\omega)\mathrm{d}\omega}}. \tag{17}$$

The wave height and zero-upcrossing period may also be evaluated with the zero-upcrossings and wave heights in time domain. Due to the linear wave profile, the quantities are similar for long time windows, but the spectral relations are more robust against noise in short time windows and therefore used in this study. The wave spectrum is calculated in encounter frequency domain. The zero-upcrossing period T_{z} is therefore not directly comparable to the zero-upcrossing period from traditional wave spectra. To enable such comparisons, the wave spectra is transformed into encounter frequency domain using the ship's forward speed v and encounter angle μ, following the method of Nielsen et al. (2021).

2.3. Identification of reliable VCG, draught estimations

In this section the selection of time windows with high accuracy is described. VCG and draught, correlation as well as wave parameters, are estimated for each time window as shown in Figs. 1–3. To identify reliable estimations, the correlation ρ, the significant wave height H_{s}, the wave zero-upcrossing period T_{z}, the roll zero-upcrossing period T_{roll}, the encounter angle μ are required from each time window.

Reliable VCG and draught estimates are selected based on five criteria:

1. The correlation ρ must exceed a minimum threshold ρ_{m}.

$$\rho > \rho_{\mathrm{m}} \tag{18}$$

2. The estimated significant wave height has to be bigger than 2 % of the breadth and smaller than 33 %.

$$0.02 < H_{\mathrm{s}}/B < 0.33 \tag{19}$$

3. The wave height to period ratio must be less than 0.5.

$$H_{\mathrm{s}}/T_{\mathrm{z}} < 0.5 \tag{20}$$

4. The maximal roll angle in the time window must exceed 2°.

$$r_{\mathrm{roll,max}} > 2^{\circ} \tag{21}$$

5. The encounter angle must not be within 10° of head or following seas.

$$|\mu| > 10^{\circ} \text{ and} |\mu - 180^{\circ}| > 10^{\circ} \tag{22}$$

These criteria reflect three qualitative requirements, where the roll motion has to be sufficiently big, but not influenced by non-linearities due to steep waves and the estimated RAO must yield a high-correlation reconstruction. The resulting estimates for VCG, D and $\hat{Y}(\omega)$ follow from averaging all selected time windows n_{c}

$$\mathrm{VCG} = \frac{1}{n_{\mathrm{c}}}\sum_{i=1}^{n_{\mathrm{c}}} \mathrm{VCG}_i, \qquad D = \frac{1}{n_{\mathrm{c}}}\sum_{i=1}^{n_{\mathrm{c}}} D_i, \qquad \hat{Y}(\omega) = \frac{1}{n_{\mathrm{c}}}\sum_{i=1}^{n_{\mathrm{c}}} \hat{Y}_i(\omega). \tag{23}$$

The accuracy of the estimation is quantified using the percentage deviation from the true draught D_{ref} and $\mathrm{VCG}_{\mathrm{ref}}$, defined as

$$\bar{\delta} = \sum_{i=1}^{n_{\mathrm{c}}} \delta_{\mathrm{i}} = \sum_{i=1}^{n_{\mathrm{c}}} \left| 1 - \frac{\mathrm{VCG_i}}{\mathrm{VCG_{ref}}} \frac{D_{\mathrm{i}}}{D_{\mathrm{ref}}} \right| \cdot 100. \tag{24}$$

The applied metric may lead to a deviation of zero, when the draught and VCG are not exactly estimated. Although, the range in which the VCG varies is greater than the draught and the formulae replicates the eigenfrequency of the ship, which increases with higher VCG and decreases with higher draught.

The peak frequency of the measured response spectrum $\omega_{\mathrm{p,ref}}$ is used to normalise and compare with the peak frequency of the calculated response spectrum ω_{p} using the wave spectrum S_ζ and the square of the selected RAO (Journée and Massie, 2001)

$$\Delta\omega_{\mathrm{p}} = \frac{|\omega_{\mathrm{p}} - \omega_{\mathrm{p,ref}}|}{\omega_{\mathrm{p,ref}}}. \tag{25}$$

The normalised peak frequency deviation is introduced to determine the accuracy of the full-scale measurements, since no VCG and draught are reported.

3. Data generation

3.1. Barge geometry

The vessel used in this study is the barge whose main dimensions are shown in Table 1 and its computational grid of the submerged part is shown in Fig. 4. It should be noted that the design draught and VCG may differ significantly from actual operating conditions, since the barge operates under variable container loading while sailing between Puerto Rico and Philadelphia (USA).

3.2. Calculation of RAOs

To apply the PSWF method, a database of RAOs is generated, as described in Section 2.3. The panel code *panFDS* solves a three-dimensional potential flow on panels and is in detail described by Söding et al. (2012) and Moctar et al. (2021). The triangular panels on the hull and quadrilateral panels on the free surface are discretized with rankine sources. The solving procedure involves two steps. First, the stationary flow problem due to the ship's forward speed is solved, returning pressures and wave elevations. Second, the numerical flow problem of the barge motion due to sea waves is conducted, while incorporating the stationary solution into the boundary conditions. As potential flow theory does not account for viscous effects, a correction is applied to the hydrodynamic damping matrix following Fossen (2011).

Table 1
Dimensions of the barge.

Parameter	Symbol	Unit	Value
Length	L	[m]	122
Breadth	B	[m]	32.2
Design draught	D	[m]	5.16
Design VCG	VCG	[m]	13.9
Block coefficient	c_b	[-]	0.85
Roll inertia radius	r_{xx}/B	[-]	0.4

Table 2
Parameter ranges for RAO database.

Parameter	Unit	Min	Max	Step
Fn	[-]	0	0.23	0.029
μ	[°]	0	350	10
VCG	[m]	9.6	24.0	1.6
D	[m]	3.84	7.41	0.51

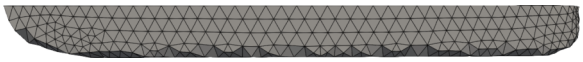

Fig. 4. Computational grid of barge used in simulations.

The database variables are defined in Table 2 and each RAO is calculated with *panFDS*. The combinations of VCG and D lead to 72 RAOs for each of the 9 Froude numbers with 36 encounter angles respectively. The absolute wave frequencies are varied for corresponding wave lengths of $0.4L$ to $5L$.

3.3. Linear motion generation

To generate idealized reference data for ship motions, first irregular waves were generated using linear wave theory and ship motions were computed using predefined RAOs. For each DOF k, the response is calculated as a sum of responses to harmonic waves, whose amplitude ζ is defined by the wave spectrum S_ζ

$$\zeta = \sqrt{2S_\zeta(\omega_{\mathrm{i}}, \mu_{\mathrm{j}})\Delta\omega\Delta\mu}. \tag{26}$$

The wave frequency ω and the encounter angle μ were equally distributed with step size $\Delta\omega$ and $\Delta\mu$ within the limits as defined in Section 3.2. The motion time series $r(t)$ was computed by taking the sum of all harmonic motions due to the number of frequencies n_ω and the number of directions n_ϕ

$$r_{\mathrm{k}}(t) = \sum_{i=1}^{n_\omega}\sum_{j=1}^{n_\phi} \mathrm{Re}\left(\hat{Y}_{\mathrm{k}}(\omega_{\mathrm{i}}, \mu_{\mathrm{j}})\sqrt{2S_\zeta(\omega_{\mathrm{i}}, \mu_{\mathrm{j}})\,\Delta\omega\,\Delta\mu}\,\exp\left(i(\omega_{\mathrm{e,i}}t - \varepsilon_{\mathrm{i,j}})\right)\right). \tag{27}$$

Due to the ship's forward speed, the motion and wave oscillate with encounter frequency $\omega_{\mathrm{e}} = \omega - \frac{v}{g}\omega^2\cos\mu$. The frequency domain solver has to be able to calculate negative encounter frequencies, e.g. stern waves. Eq. (27) can be applied to negative encounter frequencies without further modification. Each frequency and direction component was phase shifted by a uniformly distributed phase shift $\varepsilon_{\mathrm{i,j}}$ between 0 and 2π.

All simulations were performed using a short-crested Pierson-Moskowitz spectrum with 150 frequencies from 5 directions. The time step was set to 0.1 s and the total duration was one hour. The VCG was

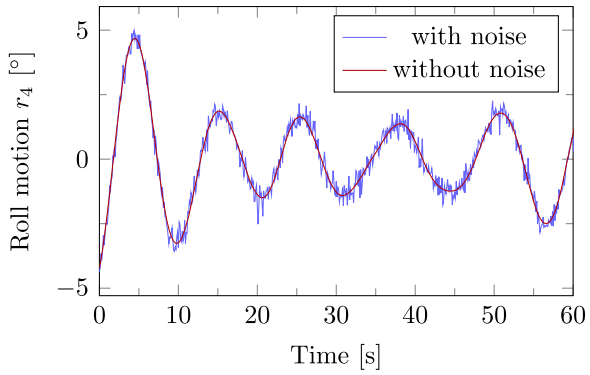

Fig. 5. Roll motion with and without noise and drift for a peak period T_p of 13 s, an encounter angle μ of 120° and a significant wave height H_s of 4 m.

set to 12.8 m, the draught to 5.89 m and the Froude number to 0.116. Variation between sea states was introduced by changing the peak wave period T_p from 3 s to 17 s with steps of 2 s and wave direction μ from 0° to 180° with steps of 30°. The significant wave height H_s was kept constant at 4 m, since Eq. (27) as well as the PSWF equations scale linearly with wave height.

3.4. Noisy linear motion generation

To generate more realistic motion time series, deviations were added to the linear motion time series described in Section 3.3. The modifications include a drift $d(t)$, noise $a_1(t)$ and deviation factors for RAO manipulation $a_2(\omega, \mu)$

$$r_k(t) = d(t) + a_1(t) + \sum_{i=1}^{n_\omega}\sum_{j=1}^{n_\phi} \mathrm{Re}\Big(a_2(\omega_i, \mu_j)\hat{Y}_k(\omega_i, \mu_j) \sqrt{2S_\zeta(\omega_i, \mu_j)\,\Delta\omega\,\Delta\mu}\, \exp\left(i(\omega_{e,i}t - \varepsilon_{i,j})\right)\Big). \tag{28}$$

The drift was a linear increase in time that reached a value of 0.001 rad after one hour

$$d(t) = 0.001 \cdot t/3600. \tag{29}$$

The noise $a_1(t)$ followed a normal distribution with zero mean and standard deviation 0.005 rad. The values were based on the actual observed noise of the installed IMUs on the full-scale barge. The deviation factors $a_2(\omega, \mu)$ were normally distributed and resulted in 95 % of all perturbations lying in the range of ±20 % of the initial value

$$a_1(t) \sim \mathcal{N}(\mu_0 = 0\,\mathrm{rad}, \sigma = 0.005\,\mathrm{rad}), \quad a_2(\omega_i, \mu_j) \sim \mathcal{N}(\mu_0 = 1, \sigma = 0.1). \tag{30}$$

Fig. 5 shows a time series for the roll motion with and without the modifications during the first minute of the simulation.

3.5. Impulse response method motions

To genereate more realistic, nonlinear motion time series, time-domain simulations using the impulse response method *IMPRES* were done. This approach enables the calculation of non-linear wave excitation forces. The equation of motion is formulated in time domain according to Cummins (1962). A detailed description of *IMPRES* and the calculation individual components can be found in Wermbter et al. (2023) and Wermbter and Abdel-Maksoud (2024)

$$(\boldsymbol{M} + \boldsymbol{A}(\infty))\ddot{\boldsymbol{r}}(t) + \boldsymbol{B}(\infty)\dot{\boldsymbol{r}}(t) + \int_0^t \boldsymbol{K}(t)\dot{\boldsymbol{r}}(t-\tau)d\tau + \boldsymbol{C}\boldsymbol{r}(t) = \boldsymbol{F}_e(t). \tag{31}$$

The individual terms are the mass matrix $\boldsymbol{M}$, the added mass matrix at infinite frequency $\boldsymbol{A}(\infty)$, the hydrodynamic damping at infinite frequency $\boldsymbol{B}(\infty)$, the matrix of retardation functions $\boldsymbol{K}(t)$, the radiation restoring matrix $\boldsymbol{C}$ and the excitation vector $\boldsymbol{F}_e(t)$. The added mass, damping and radiation restoring matrices were calculated with *panFDS*. The retardation functions were obtained by integrating the hydrodynamic damping. Excitation forces included diffraction, Froude-Krylov, restoring, roll damping, spring and Coriolis terms. The Froude-Krylov and restoring forces were updated at each time step based on the current submerged geometry, making these terms non-linear.

Simulations used a time step of 0.1 s with a total duration of one hour. As in the linear case, the configuration was set to a VCG of 12.8 m, draught of 5.89 m, and Froude number of 0.116. However, the simulations extended the range of investigated conditions, incorporating peak periods from 3 s to 17 s with steps of 1 s, encounter angles from 0° to 180° with steps of 30° and significant wave height from 2 m to 6 m with steps of 1 m. The short-crested Pierson-Moskowitz spectrum was discretized with 30 wave frequencies and 5 wave directions, yielding 150 wave components in total.

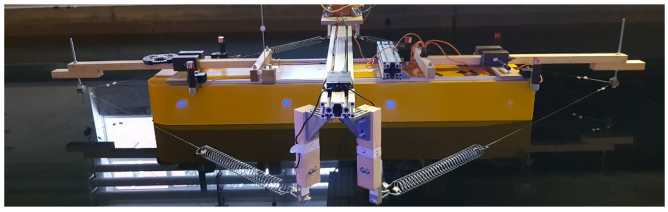

Fig. 6. Model test setup of barge model with springs.

Table 3
Model test wave conditions extrapolated to full-scale values.

H_s [m]	T_p [s]	μ [°]
4.2	10.8	45, 90, 135, 165
5.3	9.2	0, 45, 90, 135, 150, 165, 180
5.8	10.4	0, 45, 90, 135, 150, 165, 180

3.6. Model test arrangement

Model test results were conducted without forward speed using a model with a scale of 1:64 with full-scale dimensions listed in Table 1. Motions were measured via an optical tracking system and IMUs. The model motions were constrained using a spring system attached at the bow and stern, as illustrated in Fig. 6. Three long-crested Pierson-Moskowitz spectra were tested for various encounter angles, as summarized in Table 3. All measured motions, wave periods, and wave heights were scaled to full-scale conditions following Froude scaling law.

3.7. Full scale measurement data

Full-scale motion data sets were collected during measurement campaigns between July and November 2022. The barge operated between Philadelphia (USA) and Puerto Rico. Motion measurements were obtained using six IMUs, installed symmetrically on port and starboard at the bow, midship, and stern. Each IMU recorded data with a sampling frequency of 40 Hz.

GPS positions were recorded hourly and are shown on the left Fig. 7. Weather data for all GPS positions is obtained from the ERA5 database (Hersbach et al., 2020). Data within the range of 100 km of both ports were excluded to avoid inaccuracies from nearshore effects and shallow water conditions. The average ship speed was obtained from the difference in position from two consecutive GPS measurements. Measurements were partitioned into the 16 individual trips. The statistical parameters of the encountered waves with available weather report are summarized in the right subfigures of Fig. 7.

The average wave statistical parameters per trip are shown in Fig. 8. Even trip numbers indicate the barge sailing towards the USA.

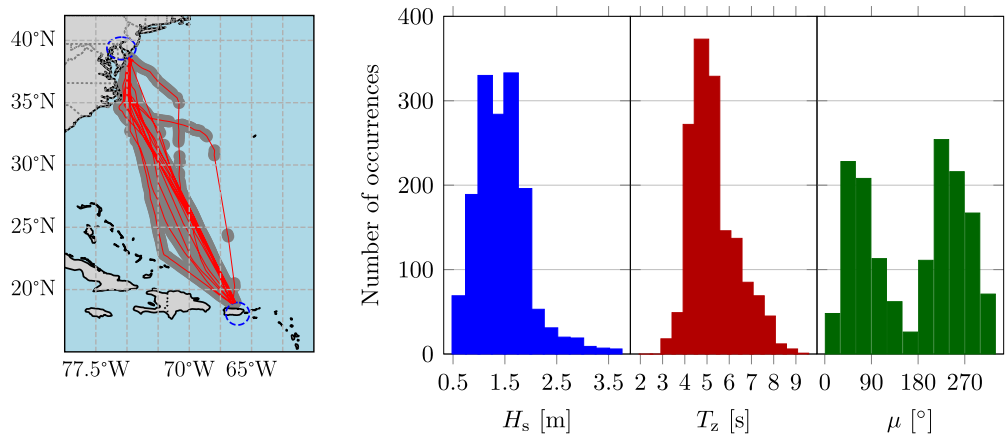

Fig. 7. Positions of barge (left) and distribution of statistical wave parameters during measurement campaign (right).

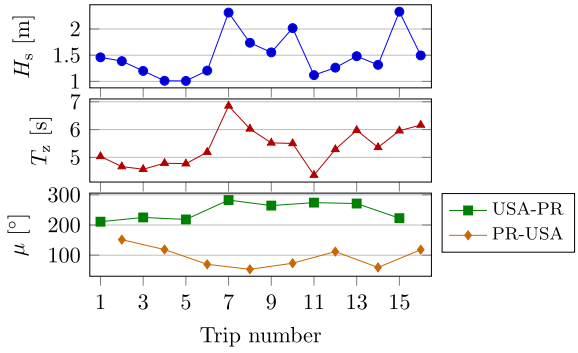

Fig. 8. Average significant wave height H_s, zero-upcrossing period T_z and heading angle μ per trip of the barge.

4. Results

4.1. Estimation with linear numerical data

In this section the procedure from Section 2 is applied to linear simulation data described in Section 3.3.

Fig. 9 shows that the proposed time series filtering from Section 2.3 filters all time windows with deviations above 5 % and results in an average deviation $\bar{\delta}$ below 1 %. The individual estimates are plotted as a function of the correlation ρ and the zero-upcrossing period ratio T_{roll}/T_z, in the following called period ratio. The correlation limit ρ_m was chosen according to the accurate estimations in Fig. 9 and used in the criteria for all following estimations. The roll zero-upcrossing period T_{roll} was evaluated from the response spectrum and Eq. (17), while the wave zero-upcrossing period T_z was derived from the estimated wave spectrum. Small period ratios led to high deviations from the target values, because they resulted in too small roll motion amplitudes. These are required to identify VCG and draught from Eq. (14), because heave and pitch RAOs do not vary as much as the roll RAO for various values of VCG and D.

Fig. 10 shows a comparison of the deviations different encounter angles using all available time windows and using only the filtered time windows. As indicated by small period ratios in Fig. 9, head and stern waves with low roll motion amplitudes result in inaccurate estimations of VCG and draught, which are unacceptably large in view of the linear input data used. However, after identifying time windows with high accuracy, these encounter angles are omitted and the remaining deviations reduce from to below 2 %. The confidence bars indicate the range, where according to the 2σ-rule, 95 % of all following estimates n_c probably would lie

$$\bar{\delta}_{95\,\%} = \bar{\delta} \pm 1.96 \frac{\sigma}{\sqrt{n_c}}. \tag{32}$$

Fig. 11 shows good agreement between the estimated RAOs for heave, roll and pitch compared with their reference RAOs at an encounter angle of 120°. The RAOs were averaged for all time windows and normalized with the wave amplitude ζ and their maximal value

$$\bar{Y}(\omega, \mu) = \frac{\hat{Y}_k(\omega, \mu)}{|\hat{Y}_{k,max}(\mu)|}. \tag{33}$$

The PSWF method allows to include arbitrary motions, moments and forces for the estimation. Torsional moments tend to have higher eigenfrequencies than the rigid-body motions (Riesner and Moctar, 2021). Fig. 12 shows the estimation performance when the torsional moment is included in the PSWF method. It reduced the deviations and allowed to make estimations for sea states with smaller wave periods, when combining with heave, roll and pitch. Although, including bending moments increased accuracy for small wave periods, the following investigations are still executed with rigid-body motions, since moment measurements are usually not available on ships.

4.2. Estimation with noisy linear numerical data

In this subsection the procedure presented in Section 2 is applied to noisy linear simulation data described in Section 3.4.

Fig. 13 shows that the noise in the motion time series did not affect the accuracy of the proposed approach and the deviation remain below 1 % and slightly increased usage to 40 %. In contrast to the noise-free case, the period ratio was not zero for time windows with negligible roll amplitudes. The motion time series, as shown in Fig. 5, with small roll motion amplitudes were amplified by the noise leading to response spectra amplitudes and a zero-upcrossing roll period greater than zero. The deviation for each encounter angle is shown in Fig. A1 and shows similar results to Fig. 10 with deviations below 2 % after time series filtering.

4.3. Estimation with impulse response method and model test data

In this section the procedure from Section 2 is applied to non-linear simulation data from the impulse response method described in Section 3.5 and model test data described in Section 3.6.

Fig. 14 shows that in contrast to linear input data, filtering was less effective reducing the deviation $\bar{\delta}$ only to around 15 % and usage to below 10 %. There is no clear separation between estimates with small deviations and high deviations, although a high correlation between reconstructed and measured motions visually indicates smaller deviations.

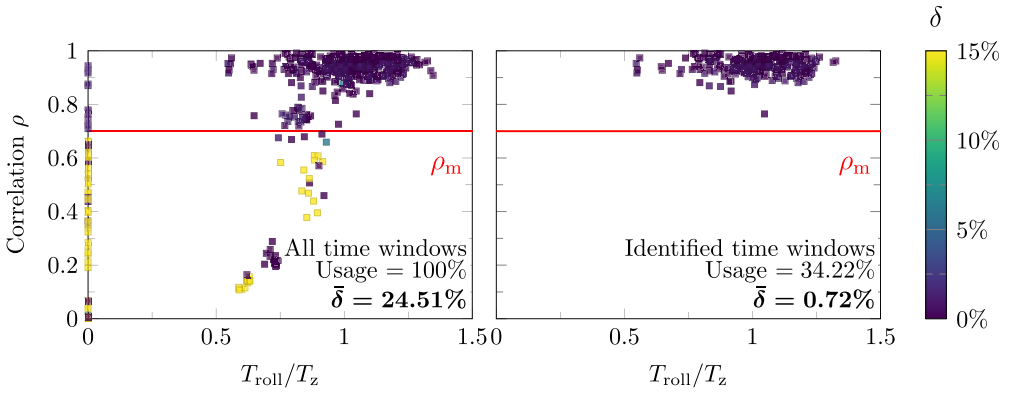

Fig. 9. Correlation ρ of reconstructed motions with measured motions plotted as function of the ratio between roll and wave zero-upcrossing period. Results are shown for all time windows (left) and for identified time windows (right). The deviation δ is indicated by color. The correlation limit ρ_m is shown by the red line.

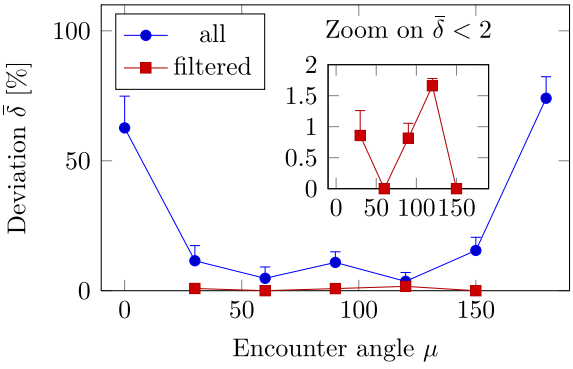

Fig. 10. Deviation from the set values plotted over encounter angle. The red curve indicates the deviation for identified time windows. The blue curve is created with all time windows. Bars indicate the 95 % confidence interval.

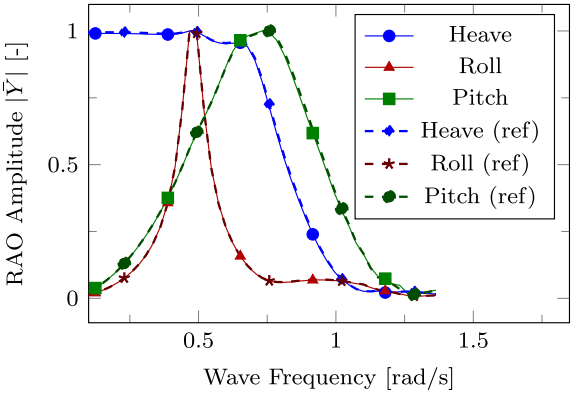

Fig. 11. Estimated RAOs for an encounter angle μ of 120° compared with the RAOs (dashed, indexed with ref) used for motion generation.

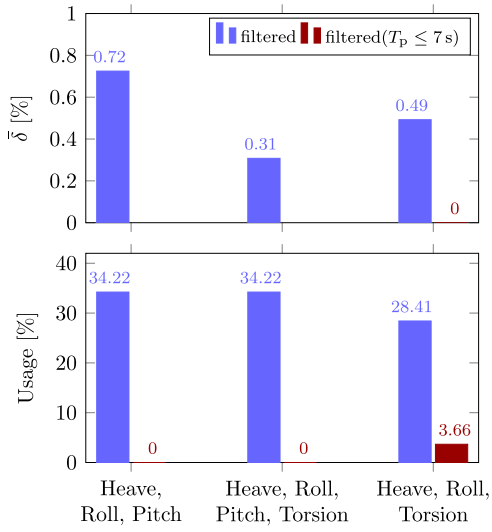

Fig. 12. Comparison of VCG and draught estimation deviation from various DOF combinations in the top. Percentage of used time windows for the estimation in the lower plot. The deviations are obtained from all time windows meeting the criteria (blue) and for all time windows meeting the criteria and a wave peak period T_p smaller or equal than 7 s (red).

Fig. 15 shows that model test deviations are coarse and around 5 %. Filtering reduced to only 4 available time windows equal to 2 % of all time windows of which one is an outlier.

Fig. 16 shows that the peak frequency deviation $\Delta\omega_p$ increases not proportionally, but similarly to the deviation for linear, noisy and impulse response data. The small number of time windows makes the estimations for model test data more accurate, but less reliable. The present results indicate that the peak frequency deviation can be a useful metric for assessing the overall estimation accuracy.

Fig. 17 shows that the estimated RAOs for heave and pitch show negligible uncertainty, whereas the roll motion shows an uncertainty of 10 % near the resonance frequency and slightly above. No reference results, as for linear data in Fig. 11, are shown since the time series are calculated by solving the equation of motion not from a RAO. Although, the deviations of VCG and draught increased to 15 %, the RAO uncertainties were small relative to their amplitudes, providing high confidence in the estimation.

Fig. 18 shows that the deviation reduces for greater zero-upcrossing periods. Furthermore, the combined metric leads to lower deviations due to contrary deviations of VCG and draught for zero-upcrossing periods around 8 s. VCG deviations and uncertainties are strongly increasing for low zero-upcrossing periods, whereas the draught deviations remain almost constant.

The probability that a seaway of the filtered time windows occurs in the next time window and is based on the encountered seaways shown in Fig. 7. It is the inverse of the probability that none of the seaways occurs

$$P = 1 - \prod_{i=1}^{n_c} (1 - P_i). \tag{34}$$

Fig. 19 shows that the correlation limit ρ_m reduces the deviations until a limit around 0.75 after which the usage is so small that confidence intervals and deviations are increasing again. Although, higher corre-

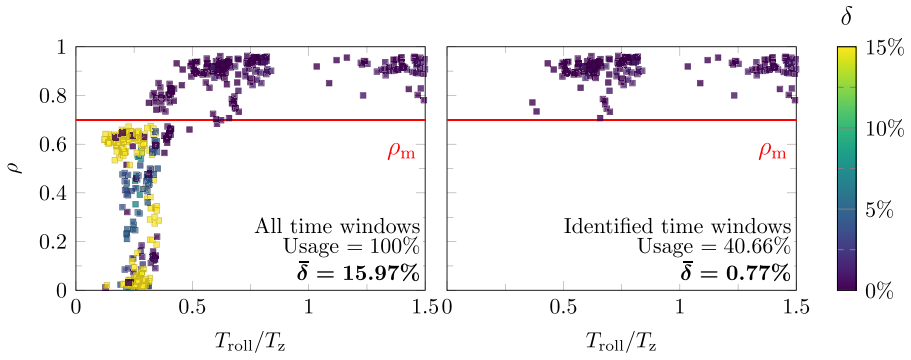

Fig. 13. Correlation of reconstructed motions with noisy linear motions. Full description in that of Fig. 9.

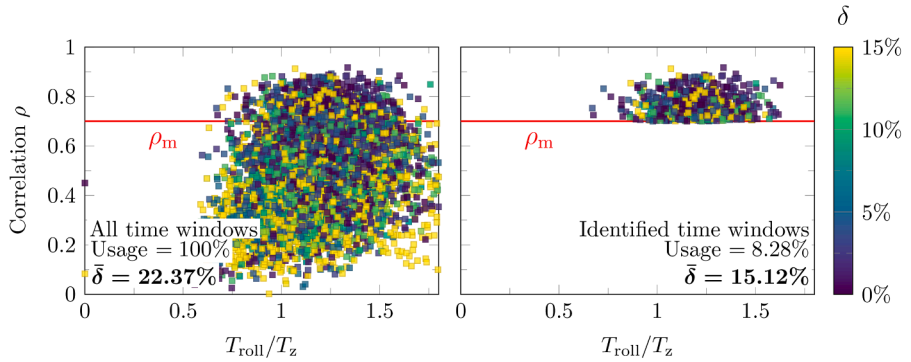

Fig. 14. Correlation of reconstructed motions with measured motions obtained from impulse response method. Full description in that of Fig. 9.

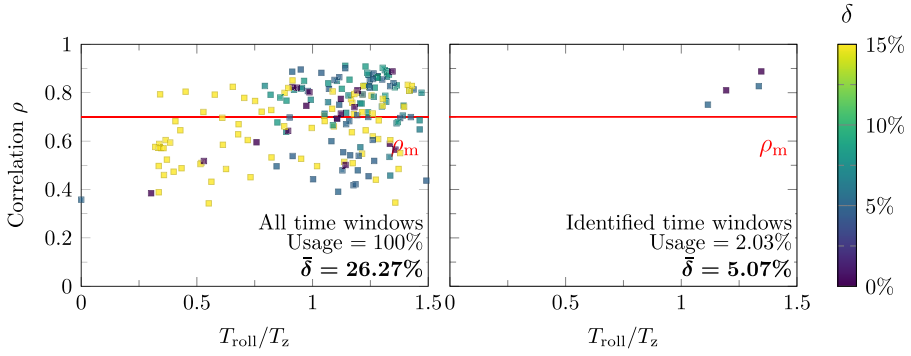

Fig. 15. Correlation of reconstructed motions with measured motions obtained from model tests. Full description in that of Fig. 9.

lations than the selected value of 0.7 yield slightly less deviation, they would limit practical feasibility, since the time until a reliable estimate is achieved increases. The confidence intervals are expected to narrow with extended datasets.

4.4. Full-scale measurement data

In this section the procedure from Section 2 is applied to full-scale measurement data described in Section 3.7.

Fig. 20 shows that peak frequency deviations $\Delta\omega_p$ varied between 7 % and 42 % during all trips, where the usage of time windows was around 10 %. Arrows indicate trips influenced by hurricanes, leading to greater peak frequency deviations than the average of the remaining trips. Excluding the hurricane influenced trips, high peak frequency deviations correlated with outliers in the estimations of VCG and draught. Higher deviations can be traced back to the wave data shown in Fig. 8, where the occurring zero-upcrossing periods were between 5 and 7 s. Zero-upcrossing periods in this range have already shown greater deviations and uncertainty with impulse response method data in Fig. 18. The ship acts as low-pass filter and the estimated peak-frequency ω_p is mostly smaller than the measured peak-frequency $\omega_{p,ref}$.

Fig. 21 shows that increasing the correlation limit ρ_m for full-scale data reduces deviations up to a correlation of 0.9, after which the number of used time windows is too small, leading to distortions in the average and uncertainty due to outliers. This trade-off highlights the need to find a balanced limit ρ_m for in-service applications, possibly even varying it during application, when it is possible to measure enough time windows with high correlation.

5. Discussion

The presented method demonstrates 2 % deviations in VCG, draught and RAO estimations with linear and noisy numerical data. Figs. 9–11 show that time series filtering is required to obtain low uncertainty, since devia-

tions arise in head and following seas or generally with motion time windows containing low roll amplitudes. Linear motions added with noise show comparable deviations to linear results showing that the method is robust against drift and noise as well as slight deviations from the RAO.

The inclusion of torsional bending moments in Fig. 12 improves the linear data estimations for low wave periods. This highlights the method's applicability even for large vessels in moderate sea conditions. A possibility to include moment RAOs in full-scale measurements using IMUs is to transform their angular velocity differences into deformation angles (Sun et al., 2007) and translate these into bending moments with differential equations for torsional and bending (Riesner and Moctar, 2021). Nevertheless, the uncertainty associated with the measurement

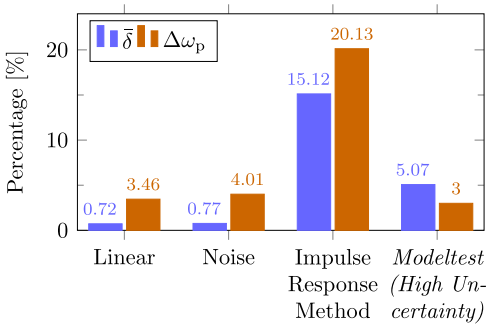

Fig. 16. Comparison of VCG, draught deviation (blue), roll peak frequency difference (orange) and usage of time windows (green) from linear, noisy, impulse response and model test motions.

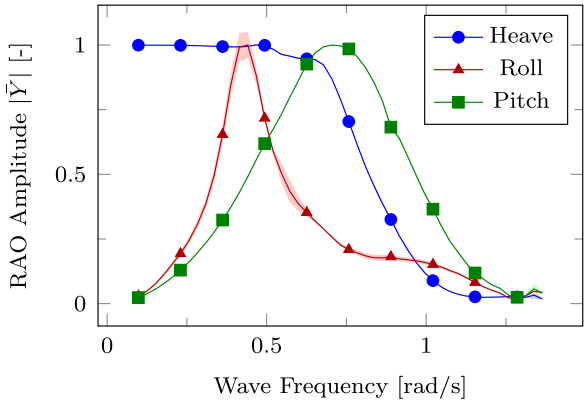

Fig. 17. Estimated RAOs for an encounter angle μ of 120° for impulse response input data. The heave (blue), roll (red) and pitch (green) RAOs as well as their confidence bands in light colors are shown.

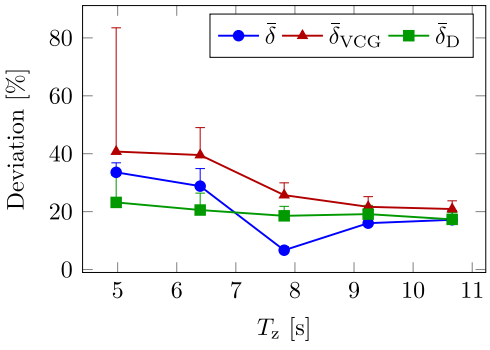

Fig. 18. Calculated deviations from impulse response input data when using solely VCG and draught deviations as well as the combined metric $\bar{\delta}$ plotted over the wave zero-upcrossing period.

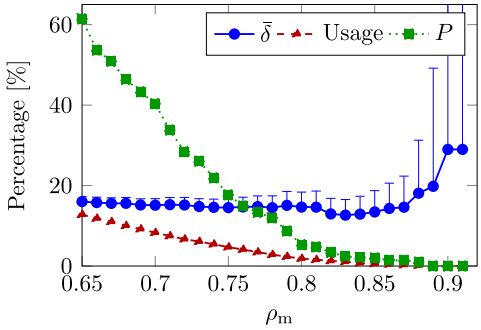

Fig. 19. Impulse response deviation $\bar{\delta}$ (blue), usage of time windows (red) and probability P along with their 95 % confidence intervals plotted against correlation limit ρ_m.

and calculation of torsional moments remains significantly higher than for rigid-body motions.

When applied to impulse response simulations and model test data, the method yielded deviations around 15 %. Comparing to results by Abankwa et al. (2018) and Javanmardi (2024) this deviations are in a similar order of magnitude, but avoid the assumption that the VCG is similar to the VCR, which is reported to deviate up to 50 % in time (Johnsen and Krüger, 2021). Results in Fig. 14 to Fig. 19 follow a similar trend, but with higher deviations as the estimations with linear data. In the case of model tests, a major limitation of the study is the small number of used time windows, which restricts statistical confidence. The filtering of almost all model test time windows can be attributed to the higher uncertainties regarding the model test measurement accuracy and RAO similarity. The waves and ship motions may be influenced by wave reflections from the tank sides and ends. The applied RAOs do not capture effects of the spring system which is mounted at the height of the deck and induces restoring forces in sway and a roll restoring moment.

Uncertainty with realistic data arises from ship motion and wave nonlinearities. Non-linearities in ship motions are not represented by a RAO, which always describe a linear dependence between wave and motion. High motion amplitudes lead to resonance frequency variations. The resulting response spectra between linear numerical data and nonlinear simulation data deviate and the estimated VCG and draught are misinterpreted due to the shifted peak frequency. Non-linearities in waves lead to higher order harmonics in the wave signal. These effects amplify for steeper waves and the resulting RAO is different from the linear case. It is expected that these effects play a role in model test and full-scale data.

Peak frequency deviations in Fig. 16 correlate to VCG, draught deviation and indicate the method's applicability to full-scale data in Figs. 20 and 21. Full-scale deviations align with the results from the linear and impulse response investigations, since the reported weather conditions fall into a period range where the method is not able to provide high accuracy as seen in Fig. 18. The peak frequency deviation may also result from errors in the reference wave spectra. Shi et al. (2024) showed that the ERA5 database may experience uncertainty in large waves as well as interference between tropical cyclones and other wave systems. Incorrect calculation of interfering wave systems can also explain the remaining deviations that are not influenced by hurricanes. Encounter angle deviations have a significant influence on the peak frequency in encounter frequency domain. Validation against datasets where VCG and draught are known will further assess the method's reliability under full-scale conditions. Additionally, the filtering and integration of ship motions described in Section 2.1 may not be sufficient to obtain accurate motions under varying motion and sea states. Small motion amplitudes are hard to measure accurately, which may lead to larger deviations in the estimated RAOs.

The uniformly discretized database of RAOs may be optimized to reduce uncertainty. An investigation into more effective discretization strategies

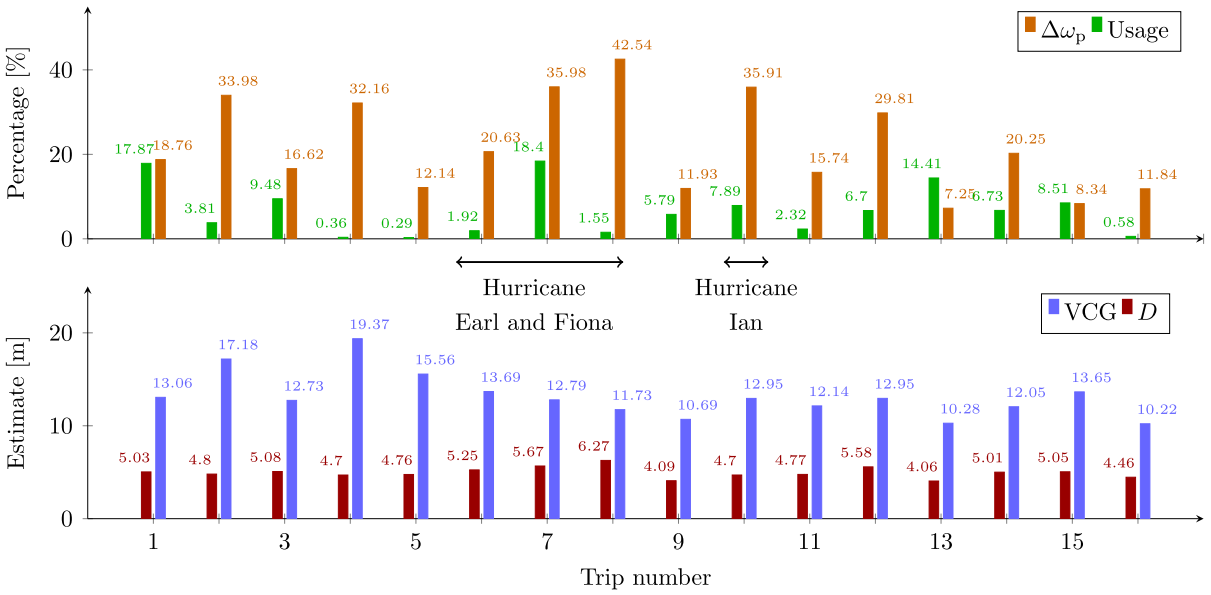

Fig. 20. Response spectrum peak frequency deviation (orange) and usage of time windows (green) in the top plot for the full-scale measurement campaign. Estimated values for VCG (blue) and draught (red) in the lower plot. Data is visualized for several trips, hurricanes influencing the estimations are marked with arrows.

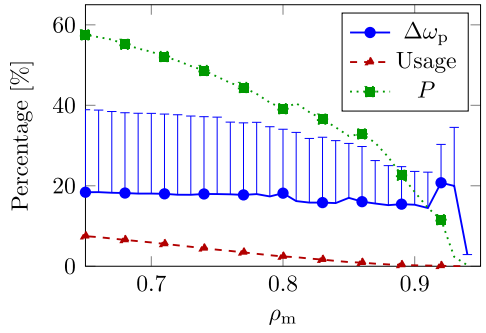

Fig. 21. Full scale peak frequency difference (blue), usage of time windows (red) and probability P along with their 95 % confidence intervals plotted against correlation limit ρ_m.

only including unique and plausible VCG and draught combinations, potentially allows to decrease database size, while avoiding outliers. It may also allow to include more parameters like radii of inertia, transversal and longitudinal center of gravity.

The applied combined metric for VCG and draught deviation $\bar{\delta}$ is more suited than individual deviations to evaluate the similarity of resulting RAOs. Fig. 18 shows that errors cancel out if VCG and draught are contrary to the reference values. However, the similarity of RAOs is well represented, because the deviation replicates the behavior of the eigenfrequency contrarily influenced by mass forces (D) and restoring forces which are influenced by the VCG, as described in Section 2.3. Additionally, the average of all estimations is closer to the real value than the average of all absolute values, therefore the deviations during application should be lower for VCG, draught and RAO than the reported absolute values for numerical investigations.

Draught may be known and reduce the problem's complexity to determination of VCG, which reduces uncertainty. Fig. 22 shows that using a fixed draught results in a deviation of 14 %. In comparison to Fig. 18 this is a reduction of the VCG deviation $\bar{\delta}_{VCG}$, which was above 20 % for all wave upcrossing periods. These results highlight that the database of RAOs should contain unique RAOs, since the available combinations in Fig. 18 lead to results which match the RAO, but don't match VCG, draught exactly.

Deviation levels of 15 % are sufficient, when the RAO is used as input for various in-service applications, but not if VCG, draught are input. Figs. 11 and 17 show that RAO deviations are less sensitive to changes in VCG and draught as the parameters themselves. Therefore, application of the estimated RAO in sea state estimations, digital twins seems feasible. When knowledge of resonance frequency and amplitude is required to determine motions, the proposed method may serve as initial guess for a numerical investigation. However, Moctar et al. (2021) state that

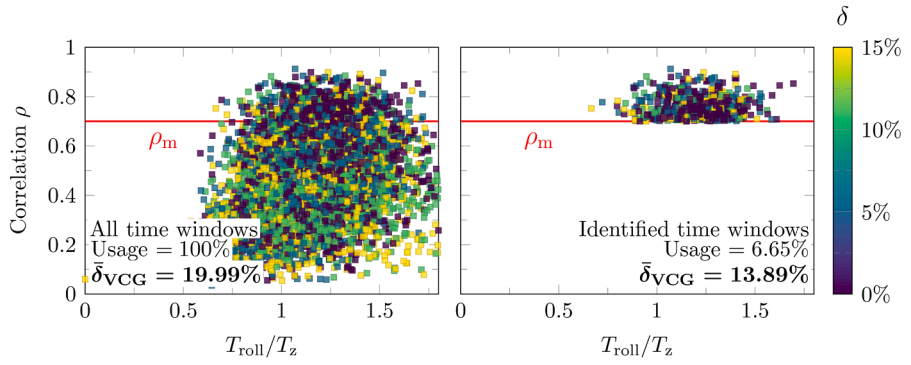

Fig. 22. Correlation of reconstructed motions with measured motions obtained from impulse response method with fixed draught of 5.89 m. Full description in that of Fig. 9.

a difference in metacentric height of 0.1 m may change the roll motion substantially and Berndt et al. (2024) showed that a 5 % change in VCG had an impact of 50 % on the logarithmic decrement, i.e. roll damping, during roll decay tests. Therefore, usage of the estimated VCG, draught as input for further calculations is not sufficient.

The method can be applied to various applications with unknown RAOs. Estimations of draught and VCG may not be superior to draught and VCG reports from the Automatic Identification System (AIS), captains or loading protocols. But if the parameters are known with sufficient precision, the method could be adapted to estimate more complex unknowns such as in-service roll damping coefficients due to marine growth, RAOs depending on wave steepness or even arbitrary RAOs. The application of the method to a database of RAOs is superior to RAO tuning methods regarding the in-service application, since the RAO is calculated for every encounter angle and frequency, whereas tuning methods are return angle dependent RAOs (Nielsen et al., 2021) or depend on the pRAO accuracy (Mounet et al., 2024). An estimation of roll damping coefficients should involve a comparison to the methodology presented by Takami et al. (2024a).

6. Conclusions

This study introduced an extension of the phase-resolved wave prediction approach using prolate spheroidal wave functions (PSWF) to estimate the vertical center of gravity (VCG), draught and RAO from measured ship motions. The methodology introduces identification criteria to select time windows with high accuracy based on the roll motion amplitude, estimated wave height and estimated wave steepness. The primary selection criterion is a minimal correlation limit between the PSWF-reconstructed motions and measured motions. Application to numerical simulations, model tests and full-scale measurements demonstrated that the approach leads to estimations with 15 % accuracy of the VCG and draught.

In addition to VCG and draught, the method enables estimation of the response amplitude operator (RAO), with deviations comparable VCG and draught at the resonance frequency of roll motion. Frequencies next to the resonance frequency as well as heave and pitch RAOs lead to negligible prediction uncertainty. To assess the validity of full-scale measurements with unknown VCG and draught, the peak frequency deviation between the measured and estimated response spectrum was compared and verified to result in comparable deviations as for VCG and draught. The comparison lead to deviations from 7 % to 40 %, where the outliers may be attributed to low motion amplitudes and the influence of local weather phenomena. Further validation with full-scale measurements, where VCG and draught are known would further enhance the confidence for practical application of the method.

The current implementation is limited to the VCG and draught as parameters. Future work should investigate if accuracy levels change when the parameter space is extended. The input database of RAOs may be calculated with parameterized RAOs, such as those proposed by Jensen et al. (2004), to reduce computational cost. The database can also be extended to include additional parameters such as roll damping coefficients, wave steepness, transverse center of gravity, and others, thereby increasing the method's flexibility regarding variations in the input motions.

CRediT authorship contribution statement

Malwin Wermbter: Writing - review & editing, Writing - original draft, Visualization, Validation, Software, Methodology, Investigation, Formal analysis, Data curation, Conceptualization; **Robinson Perić:** Writing - review & editing, Visualization, Validation, Methodology, Investigation, Conceptualization; **Johanna Serr:** Writing - review & editing, Visualization, Methodology, Investigation, Formal analysis, Data curation, Conceptualization; **Moustafa Abdel-Maksoud:** Writing - review & editing, Supervision, Resources, Project administration, Methodology, Funding acquisition, Conceptualization.

Data availability

The source code for the analysis is available on GitLab: https://collaborating.tuhh.de/m-8/rao_estimator.

Declaration of generative AI and AI-assisted technologies in the writing process

During the preparation of this work the authors used ChatGPT in order to act as a virtual reviewer and assist with rewriting and improving the clarity of the manuscript during the first draft. After using this tool, the authors reviewed and edited the content as needed and take full responsibility for the content of the published article.

Declaration of competing interest

The authors declare that they have no known competing financial interests or personal relationships that could have appeared to influence the work reported in this paper.

Acknowledgment

This work was supported by the Bundeswehr Technical Center for Ships and Naval Weapons Maritime Technology and Research; the German Federal Ministry for Economic Affairs and Energy under contract 03SX596B administrated by the Project Management Jülich.

Appendix A.

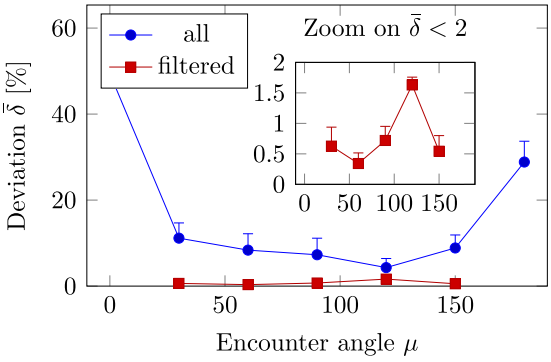

Fig. A1. Deviation from the set values for noisy linear motions plotted over encounter angles. Full description in that of Fig. 10.

References

Abankwa, N.O., Bowker, J., Johnston, S.J., Scott, M., Cox, S.J., 2018. Estimating the longitudinal center of flotation of a vessel in waves using acceleration measurements. IEEE Sens. J. 18 (20), 8426–8435. https://doi.org/10.1109/jsen.2018.2865463

Al-Rawashdeh, Y., Elshafei, M., Al-Malki, M., 2014. In-flight estimation of center of gravity position using all-accelerometers. Sensors 14 (9), 17567–17585. https://doi.org/10.3390/s140917567

Al-Rawashdeh, Y.M., Elshafei, M., Ouakad, H., 2023. Mass and inertia estimation using all-accelerometer. In: 2023 IEEE Sensors Applications Symposium (SAS). IEEE. https://doi.org/10.1109/sas58821.2023.10254165

Berndt, J., Peric, R., Abdel-Maksoud, M., Park, S., Rosenblum, K., Sanada, Y., Stern, F., Tonelli, R., Toxopeus, S., Hamstad, T., 2024. Performing and documenting flow simulations andexperiments of roll-decay tests and the comparison of theirresults. In: 35th Symposium on Naval Hydrodynamics Nantes, France, 8 - 12 July, 2024.

Boyd, J.P., 2005. Algorithm 840: computation of grid points, quadrature weights and derivatives for spectral element methods using prolate spheroidal wave functions—prolate elements. ACM Trans. Math. Software 31 (1), 149–165. https://doi.org/10.1145/1055531.1055538

Chhoeung, S., Hahn, A., 2019. Approach to estimate the ship center of gravity based on accelerations and angular velocities without ship parameters. J. Phys. Conf. Ser. 1357, 012028. https://doi.org/10.1088/1742-6596/1357/1/012028

Cummins, W.E., 1962. The Impulse Response Function and Ship Motions. Technical Report. David Taylor Model Basin Washington DC.

de Oliveira, C.D., Fernandes, A.C., Sales Junior, J.S., Asgari, P., 2018. Instantaneous center of rotation in pitch response of a FPSO submitted to head waves. In: Volume 7A: Ocean Engineering. American Society of Mechanical Engineers. https://doi.org/10.1115/omae2018-78098

Fathy, H.K., Kang, D., Stein, J.L., 2008. Online vehicle mass estimation using recursive least squares and supervisory data extraction. In: 2008 American Control Conference. IEEE. https://doi.org/10.1109/acc.2008.4586760

Fernandes, A.C., Asgari, P., Soares, A. R.W., 2016. Asymmetric roll center of symmetric body in beam waves. Ocean Eng. 112, 66–75. https://doi.org/10.1016/j.oceaneng.2015.12.001

Fossen, T.I., 2011. Handbook of Marine Craft Hydrodynamics and Motion Control. Wiley. https://doi.org/10.1002/9781119994138

Han, X., Leira, B.J., Sævik, S., 2021. Vessel hydrodynamic model tuning by discrete Bayesian updating using simulated onboard sensor data. Ocean Eng. 220, 108407. https://doi.org/10.1016/j.oceaneng.2020.108407

Hersbach, H., Bell, B., Berrisford, P., Hirahara, S., Horányi, A., Muñoz-Sabater, J., Nicolas, J., Peubey, C., Radu, R., Schepers, D., Simmons, A., Soci, C., Abdalla, S., Abellan, X., Balsamo, G., Bechtold, P., Biavati, G., Bidlot, J., Bonavita, M., De Chiara, G., Dahlgren, P., Dee, D., Diamantakis, M., Dragani, R., Flemming, J., Forbes, R., Fuentes, M., Geer, A., Haimberger, L., Healy, S., Hogan, R.J., Hólm, E., Janisková, M., Keeley, S., Laloyaux, P., Lopez, P., Lupu, C., Radnoti, G., de Rosnay, P., Rozum, I., Vamborg, F., Villaume, S., Thépaut, J., 2020. The ERA5 global reanalysis. Q. J. R. Meteorolog. Soc. 146 (730), 1999–2049. https://doi.org/10.1002/qj.3803

Javanmardi, M., 2024. Estimation of vessel center of gravity using inertial measurement units in random waves for enhanced navigational safety. Int. J. Offshore Polar Eng. 34 (4), 440–447. https://doi.org/10.17736/ijope.2024.su03

Jensen, J.J., Mansour, A.E., Olsen, A.S., 2004. Estimation of ship motions using closed-form expressions. Ocean Eng. 31 (1), 61–85. https://doi.org/10.1016/s0029-8018(03)00108-2

Johnsen, L., Krüger, S., 2021. Determination of the vertical location of the axis of rotation of the roll motion from full-scale measurements. In: Volume 6: Ocean Engineering. American Society of Mechanical Engineers. https://doi.org/10.1115/omae2021-62301

Journée, J., Massie, W., 2001. Offshore Hydromechanics. Delft University of Technology 523.

Kitagawa, G., 2010. Introduction to Time Series Modeling. Chapman and Hall/CRC. https://doi.org/10.1201/9781584889229

Mak, B., Düz, B., 2019. Ship as a wave buoy: estimating relative wave direction from in-service ship motion measurements using machine learning. In: Volume 9: Rodney Eatock Taylor Honoring Symposium on Marine and Offshore Hydrodynamics; Takeshi Kinoshita Honoring Symposium on Offshore Technology. American Society of Mechanical Engineers. https://doi.org/10.1115/omae2019-96201

Mittendorf, M., Nielsen, U., Bingham, H., Storhaug, G., 2022. On the determination of the relative wave direction based on measured ship responses using deep multi-task learning. In: 14th International Symposium on High-Performance Marine Vehicles (HIPER'22).

Moctar, B. O.e., Schellin, T.E., Söding, H., 2021. Numerical Methods for Seakeeping Problems. Springer International Publishing. https://doi.org/10.1007/978-3-030-62561-0

Mounet, R. E.G., Nielsen, U.D., Brodtkorb, A.H., Øveraas, H., Dallolio, A., Johansen, T.A., 2024. Data-driven method for hydrodynamic model estimation applied to an unmanned surface vehicle. Measurement 234, 114724. https://doi.org/10.1016/j.measurement.2024.114724

Nielsen, U.D., Mounet, R. E.G., Brodtkorb, A.H., 2021. Tuning of transfer functions for analysis of wave-ship interactions. Mar. Struct. 79, 103029. https://doi.org/10.1016/j.marstruc.2021.103029

Perez, T., 2006. Ship Motion Control: Course Keeping and Roll Stabilisation Using Rudder and Fins. Springer Science & Business Media.

Riesner, M., Moctar, O.e., 2021. A numerical method to compute global resonant vibrations of ships at forward speed in oblique waves. Appl. Ocean Res. 108, 102520. https://doi.org/10.1016/j.apor.2020.102520

Shi, J., Feng, X., Toumi, R., Zhang, C., Hodges, K.I., Tao, A., Zhang, W., Zheng, J., 2024. Global increase in tropical cyclone ocean surface waves. Nat. Commun. 15 (1). https://doi.org/10.1038/s41467-023-43532-4

Stanley, A., Goodall, R., 2009. Estimation of aircraft centre of gravity using Kalman filters. In: 2009 European Control Conference (ECC). IEEE. https://doi.org/10.23919/ecc.2009.7074672

Sun, F., Guo, C., Gao, W., Li, B., 2007. A New Inertial Measurement Method of Ship Dynamic Deformation. IEEE. pp. 3407–3412. https://doi.org/10.1109/icma.2007.4304110

Söding, H., von Graefe, A., Moctar, O.e., Shigunov, V., 2012. Rankine source method for seakeeping predictions. In: Volume 4: Offshore Geotechnics Ronald W. Yeung Honoring Symposium on Offshore and Ship Hydrodynamics. American Society of Mechanical Engineers. https://doi.org/10.1115/omae2012-83450

Takami, T., Dam Nielsen, U., Juncher Jensen, J., Maki, A., Matsui, S., Komoriyama, Y., 2024a. Onboard identification of stability parameters including nonlinear roll damping via phase-resolved wave estimation using measured ship responses. Mech. Syst. Signal Process. 210, 111166. https://doi.org/10.1016/j.ymssp.2024.111166

Takami, T., MounetR. E., NielsenU. D., 2024b. Phase-resolved estimation of ship transfer functions using response measurements. In: Proceedings of the 2024 Annual Autumn Meeting of JASNAOE, pp. 57–64.

Takami, T., Nielsen, U.D., Jensen, J.J., Chen, X., 2023. Estimation of encountered wave elevation sequences based on response measurements in multi-directional seas. Appl. Ocean Res. 135, 103570. https://doi.org/10.1016/j.apor.2023.103570

Takami, T., Nielsen, U.D., Mounet, R. E.G., Jensen, J.J., Mori, R., Komoriyama, Y., 2025. Data-driven estimations of response transfer functions of a marine vessel and phase-resolved incident waves . https://doi.org/10.2139/ssrn.5122331

Takami, T., Nielsen, U.D., Xi, C., Jensen, J.J., Oka, M., 2022. Reconstruction of incident wave profiles based on short-time ship response measurements. Appl. Ocean Res. 123, 103183. https://doi.org/10.1016/j.apor.2022.103183

Wermbter, M., Abdel-Maksoud, M., 2024. Calculation of ship motions in steep waves with restoring and Froude-Krylov forces on an adaptive panel mesh with Gauss and analytic integration methods. J. Hydrodyn. 36 (2), 275–289. https://doi.org/10.1007/s42241-024-0026-6

Wermbter, M., Altenbach, L., Detlefsen, O., Abdel-Maksoud, M., 2023. Comparative summary of approaches used with the impulse response method. IOP Conference Series: Materials Science and Engineering 1288 (1), 012024. https://doi.org/10.1088/1757-899x/1288/1/012024

Wittmer, K., Sawodny, O., Henning, K.-U., 2023. Model-based estimation of vehicle center of gravity height and load. J. Dyn. Syst. Meas. Control 145 (5). https://doi.org/10.1115/1.4056987

Zhang C., 2022. Sensor Integration for Ship Motion Analysis. Ph.D. thesis. Universität Oldenburg. http://oops.uni-oldenburg.de/5474/.